Article

Unveiling the Antiviral Capabilities of Targeting Human Dihydroorotate Dehydrogenase against SARS-CoV-2

Aline D. Purificação, Sabrina Silva-Mendonça, Luiza V. Cruz, Carolina Q. Sacramento, Jairo R. Temerozo, Natalia Fintelman-Rodrigues, Caroline Souza de Freitas, Bruna Fleck Godoi, Miguel Menezes Vaidergorn, Juliana Almeida Leite, Luis Carlos Salazar Alvarez, Murillo V. Freitas, Meryck F. B. Silvac, Bianca A. Martin, Renata F. V. Lopez, Bruno J. Neves, Fabio T. M. Costa, Thiago M. L. Souza, Flavio da Silva Emery, Carolina Horta Andrade,* and M. Cristina Nonato*

Read Online

ACCESS | Metrics & More | Article Recommendations | SI Supporting Information

ABSTRACT: The urgent need for effective treatments against emerging viral diseases, driven by drug-resistant strains and new viral variants, remains critical. We focus on inhibiting the human dihydroorotate dehydrogenase (*Hs*DHODH), one of the main enzymes responsible for pyrimidine nucleotide synthesis. This strategy could impede viral replication without provoking resistance. We evaluated naphthoquinone fragments, discovering potent *Hs*DHODH inhibition with IC_{50} ranging from 48 to 684 nM, and promising *in vitro* anti-SARS-CoV-2 activity with EC_{50} ranging from 1.2 to 2.3 μM. These compounds exhibited low toxicity, indicating potential for further development. Additionally, we employed computational tools such as molecular docking and quantitative structure−activity relationship (QSAR) models to analyze protein−ligand interactions, revealing that these naphthoquinones exhibit a protein binding pattern similar to brequinar, a potent *Hs*DHODH inhibitor. These findings represent a significant step forward in the search for effective antiviral treatments and have great potential to impact the development of new broad-spectrum antiviral drugs.
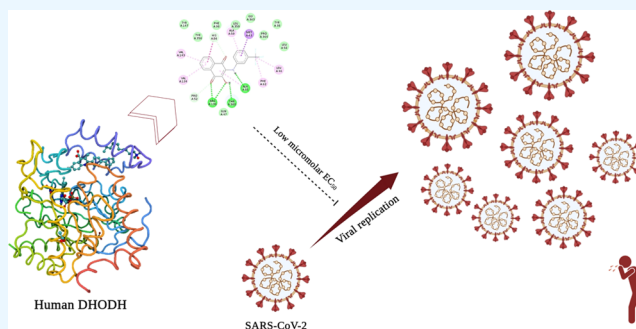
INTRODUCTION

Since the first evidence of COVID-19 in December 2019, the world has suffered the devastating consequences of the pandemic caused by SARS-CoV-2, resulting in more than 770 million confirmed cases and almost 7 million deaths as of November 29, 2023.[1] Since the early alerts, various professionals have exerted efforts to contain the pandemic, advancing research in the areas of public health control, hospital procedures, and research and development. In the field of research and development, two main approaches have been adopted: the development of vaccines as a means of preventing infection and the development of treatments to address those already infected.

With the development of initial vaccines and mass vaccination efforts, the overall landscape of the pandemic has shifted significantly. Vaccination has proven crucial in reducing the number of COVID-19 cases, hospitalizations, and deaths.[2,3] However, vaccine coverage does not reach everyone, particularly those in more vulnerable socioeconomic conditions.[4] Additionally, even vaccinated individuals may require medical intervention and, at times, hospitalization. Therefore,

safe and effective treatment is also a necessary tool against COVID-19.

In this context, the search for therapeutic options for COVID-19 remains an intriguing strategy. Throughout the pandemic, it has been essential for mitigating the number of deaths by utilizing both drug discovery and drug repositioning. Drug repositioning allowed the approval of different small-molecule drugs, generally broad-spectrum antivirals such as Remdesivir[5−7] that was initially developed to treat the Ebola Virus. Another commercially available drug for rheumatoid arthritis, leflunomide, has been extensively studied for its potential anti-SARS-CoV-2 action.[8−11] Leflunomide is a prodrug, and its active metabolite, teriflunomide, is a potent inhibitor of the human dihydroorotate dehydrogenase
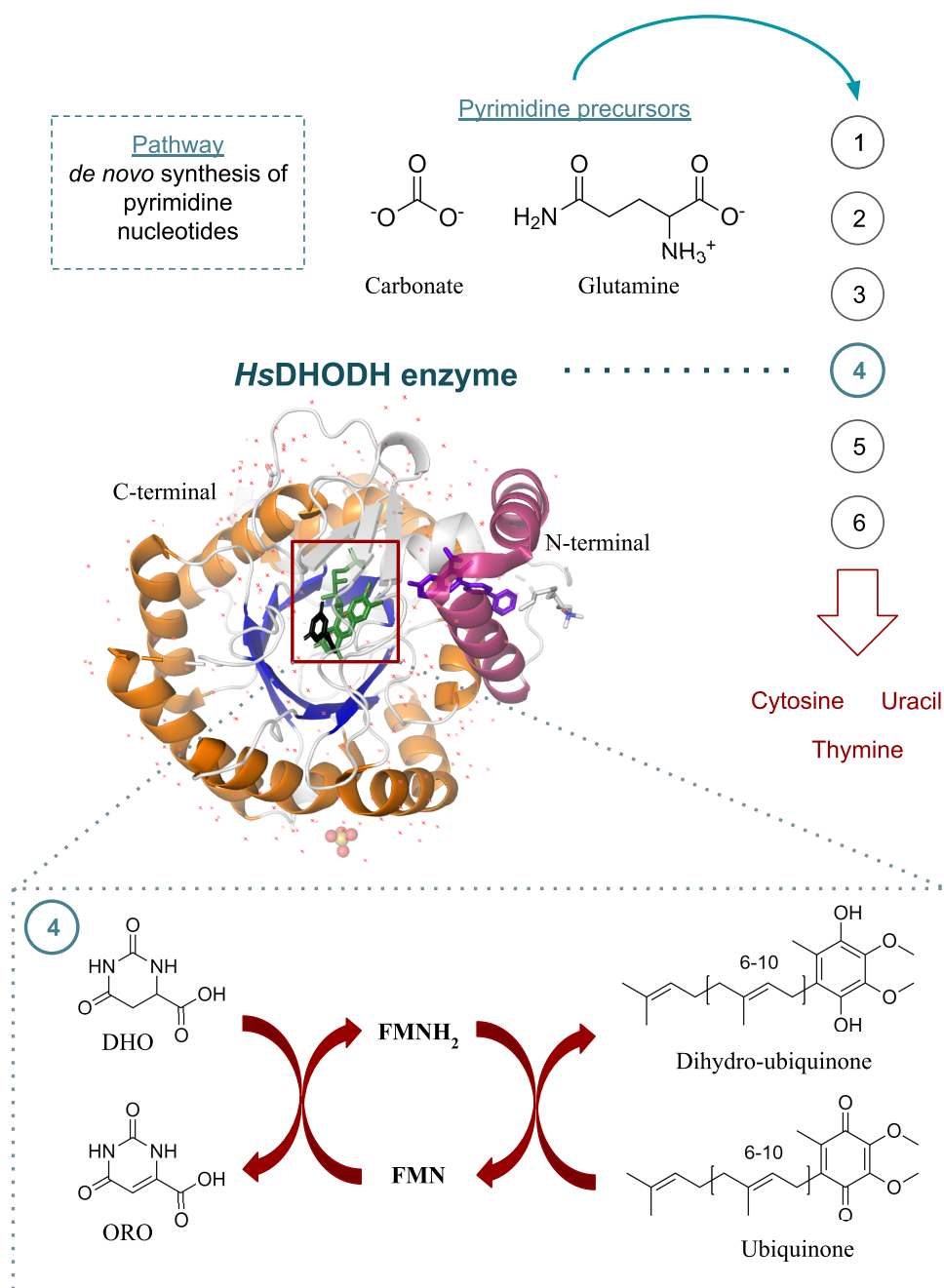
Figure 1. *Hs*DHODH is part of the *de novo* pyrimidine biosynthesis. The synthesis of pyrimidine nucleotides relies on the precursors carbonate and glutamine and involves six steps catalyzed by carbamoyl phosphate synthetase (step 1), aspartate transcarbamylase (step 2), dihydroorotase (step 3), dihydroorotate dehydrogenase (step 4), and the bifunctional enzyme UMP synthase, which is involved in the final two steps. The *Hs*DHODH enzyme plays a key role in the fourth step of the synthesis, catalyzing an oxireduction reaction via a ping-pong mechanism that converts dihydroorotate (DHO) to orotate (ORO) using monoflavin FMN as a cofactor, which is then recovered by the ubiquinone molecule. This pathway is essential for maintaining an adequate supply of intracellular pyrimidine nucleotides.

(*Hs*DHODH), which participates in the *de novo* synthesis of pyrimidine nucleotides.

The *de novo* synthesis of pyrimidine nucleotides is a pathway conserved across bacteria,[12,13] protozoan,[14] animals,[15−17] and plants,[18] supplying the basic building blocks for the nucleic acids DNA and RNA. Recently, this pathway has been studied as a target for broad-spectrum antivirals since viruses rely on specific host factors to complete its life cycle.[19]

Cells with high replication rates, such as those involved in viral replication, have a greater demand for nucleotides compared to slowly replicating cells, including most adult human cells.[20] Thus, targeting key enzymes involved in host nucleotide biosynthesis represents a promising broad-spectrum antiviral strategy.[21,22] By inhibiting these enzymes, we can disrupt the availability of nucleotides that are crucial for viral replication, thereby impeding the viral life cycle and proliferation within the host cell.

Dihydroorotate dehydrogenases are involved in the *de novo* biosynthesis of pyrimidines, responsible for the fourth step, a redox rate-limiting step in the pathway.[23] Located on the outer surface of the inner membrane of mitochondria, *Hs*DHODH converts dihydroorotate to orotate, subsequently utilized to

Table 1. The Activity of the Tested Quinones Regarding Enzyme Inhibition, Anti-SARS-CoV-2 Activity, and Cytotoxicity[a]

	IC_{50}, nM	EC_{50}, μM	CC_{50}, μM (HepG2)	CC_{50}, μM (Calu-3)	selectivity index
lapachol	48 ± 4	1.5 ± 0.1	71 ± 9	67 ± 2	47 ± 7
QHM011	680 ± 50	2.3 ± 0.3	180 ± 20	77 ± 2	80 ± 10
QHM020	290 ± 30	1.8 ± 0.2	60 ± 10	75 ± 2	35 ± 7
QHM034[b]	360 ± 20	ND	320 ± 90	ND	ND
QHM110	101 ± 3	1.5 ± 0.2	180 ± 30	48 ± 2	120 ± 30
QHM230	470 ± 30	1.2 ± 0.2	140 ± 30	67 ± 2	110 ± 30
QHM297[c]	310 ± 50	ND	17 ± 4	ND	ND
ML390	200 ± 10	ND	16 ± 5	91 ± 2	ND
brequinar	5.5 ± 0.5	0.8 ± 0.1	17 ± 4	48 ± 2	20 ± 5
teriflunomide	145 ± 4	ND	160 ± 20	59 ± 2	ND
remdesivir	NA	0.08 ± 0.02	NA	NA	NA

[a]Table presents the in vitro values for enzyme inhibition (IC_{50} in *Hs*DHODH), anti-SARS-CoV-2 activity (EC_{50} in infected Calu-3 cells), and cytotoxicity (CC_{50} in both HepG2 and Calu-3 cells) of the tested quinones and experimental controls. The selective index for each compound is also reported, representing the correlation between its anti-SARS-CoV-2 activity and HepG2 cytotoxicity. All values are displayed as mean ± standard error; ND indicates not available data; NA indicates not applicable data [b]Compound chemically unstable. [c]Due to the high toxicity observed in HepG2 cell lines, this compound was not assessed in Calu-3 cell experiments.
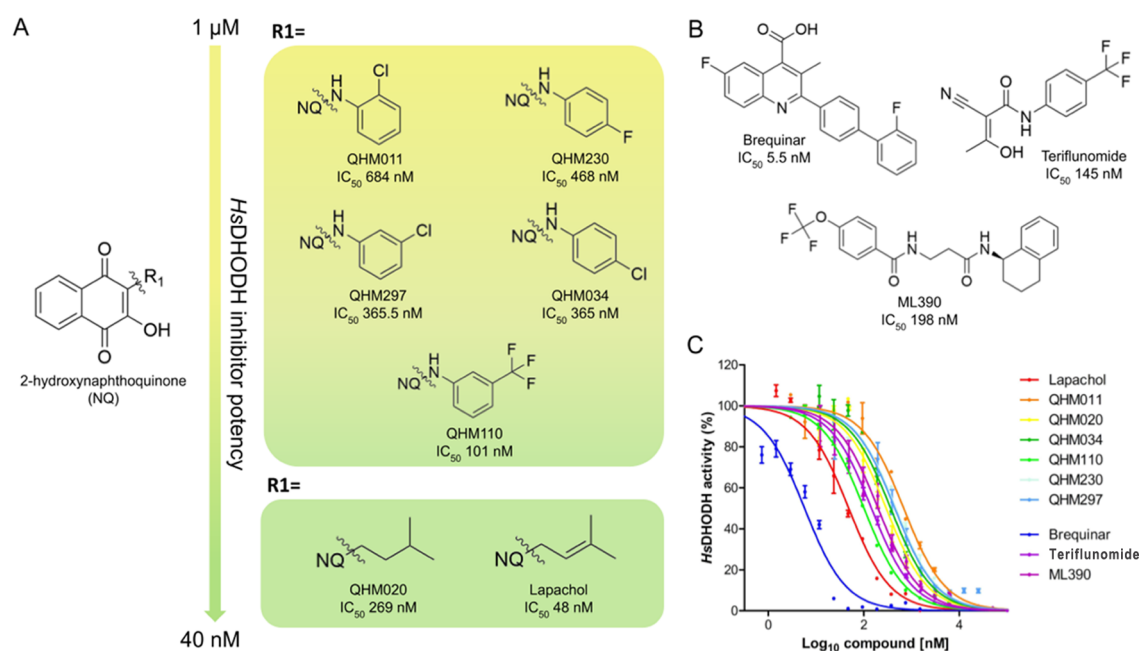

Figure 2. Naphthoquinones are potent *Hs*DHODH inhibitors. The structures and dose−response curves of enzymatic inhibition for the tested compounds are shown. (A) The structures of the 3-alkyl-substituted-NQ and 3-isopentyl 3-substitute-NQ series are sorted by potency against *Hs*DHODH, ranging from 1 μM to 40 nM. (B) The chemical structures of the commercial and clinical *Hs*DHODH inhibitors, including brequinar, terifluonomide, and ML390, are shown. (C) The IC_{50} curves for all of the quinones tested in this study, as well as the experimental controls, are presented.

produce uridine monophosphate (UMP) and, finally, pyrimidine nucleotide[23−25] (Figure 1).

The inhibition of pyrimidine biosynthesis targeting *Hs*DHODH has been utilized as a therapeutic target in various fields, including rheumatology,[26] oncology,[27,28] immunological disorders,[29] and infectious diseases,[8,19,22,30−37] due to its immunomodulatory properties. The extensively studied natural naphthoquinone lapachol is known as a potent inhibitor of *Hs*DHODH and has been studied for example in arthritis, cancer, bacterial, and viral infectious.[38] In this study, we assessed the inhibitory potential of a small group of naphthoquinone compounds, akin to lapachol, against *Hs*DHODH and their in vitro anti-SARS-CoV-2 activity. The compounds demonstrated potency against the enzyme as well as against SARS-CoV-2, with IC_{50} values in the nanomolar

range and EC_{50} values in the micromolar range. Furthermore, these compounds exhibited low cytotoxicity. To analyze protein−ligand interactions and identify the fragments responsible for the antiviral activity, we employed computational approaches, including molecular docking and quantitative structure−activity relationship (QSAR) models. These findings provide valuable insights for future hit-to-lead optimization campaigns.

■ RESULTS AND DISCUSSION

In a previous study, our group developed various quinoidal compounds derived from the atovaquone ring aiming to target *Schistosoma mansoni* DHODH (*Sm*DHODH).[39] As this enzyme falls under the class 2 DHODH category, it shares structural and sequential elements with *Hs*DHODH. With the
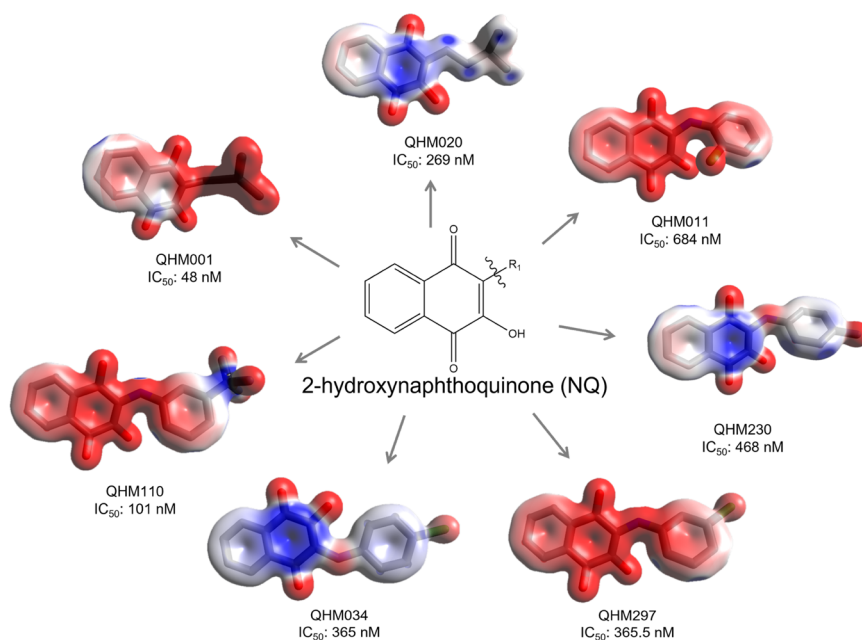
Figure 3. Electrostatic potential map of tested quinones. The diagram illustrates the electrostatic differences between compounds and their relationship to IC_{50} values. Compounds are presented in stick models, with carbon atoms in gray, hydrogen in white, oxygen in red, nitrogen in blue, chlorine in green, and fluorine in light blue. The electrostatic potential is represented as the electron density of the atoms, where red, blue, and white indicate negative, positive, and neutral potential, respectively.

intention of employing these compounds as antiparasitic agents, there is concern regarding their selectivity for the *S. mansoni* enzyme in comparison to its human homologue. Therefore, we systematically assessed the efficacy of these compounds against *Sm*DHODH, using *Hs*DHODH as a reference to appraise their selectivity for the parasite enzyme. While some compounds exhibited significant activity against *Sm*DHODH, a subset among them lacked selectivity and also demonstrated high potency in inhibiting *Hs*DHODH. Therefore, in this study, with *Hs*DHODH as the target, we revalidated seven of these naphthoquinoidal fragments that proved to be potent inhibitors of *Hs*DHODH. We assessed their enzymatic inhibition and, for the first time, evaluated their experimental anti-SARS-CoV-2 activity and cytotoxicity data (Table 1 and Figure 2). As experimental controls, we used the *Hs*DHODH inhibitors brequinar, teriflunomide, and ML390, which all fell within the nanomolar range (Figure 2). The tested compounds belong to the class of 2-hydroxynaphthoquinones (NQ) and can be classified into two groups based on their chemical structure. The first group comprises 3-alkyl-substituted NQ, which includes lapachol with an isoprenyl chain and reduced lapachol (QHM020) with a 3-isopentyl 3-substituted-NQ. The second group is a series of 3-anilines-NQ (Figure 2).

The most potent compound tested for the *Hs*DHODH inhibition was lapachol, which had an IC_{50} value of 48 nM. Interestingly, when the isoprenyl chain of lapachol was reduced (QHM020), the inhibitory potential decreased by approximately 5-fold (Table 1 and Figure 2). The isopentyl portion of QHM020 is more flexible, less lipophilic, and less electronegative than the allyl group. The difference in IC_{50} values for lapachol and QHM020 suggests that these properties may guide the potency of the compounds in *Hs*DHODH. However, the similarity in IC_{50} values for QHM020 and compounds of the 3-anilines-NQ series, such as QHM110, QHM034, and QHM297, which have a bulkier R1 (Figure 2), strongly

suggests that differences in molecular volume do not impact enzyme inhibition.

Upon examination of compounds QHM034, QHM297, and QHM230, it becomes evident that chloride and fluoride in para- or meta-substituted anilines have similar effects on enzyme inhibition (Table 1 and Figure 2). Thus, differences in the physicochemical properties of halogens, such as electronegativity and atomic radius, do not appear to impact enzyme inhibition. However, the halogen in the ortho position is less favorable (QHM011) compared to the meta- and para-substituted benzene (QHM230, QHM297, QHM034).

Interestingly, replacing a halogen with a bulky trifluoromethyl group (QHM110) resulted in a significant increase in potency (Table 1 and Figure 2). Notably, QHM110 shares similarities with teriflunomide (IC_{50} = 145 nM), which also possesses the trifluoromethyl group in the para-benzene position. This similarity is evident in the superposition of both structures in *Hs*DHODH, as illustrated in Figure S1.

To better understand how these compounds interact with *Hs*DHODH and elicit structure−activity relationships (SAR), we conducted molecular docking for each compound with this enzyme. Additionally, we calculated the electrostatic potential map for quinones (Figure 3). The Glide XP Scores, Ligand Efficiency (LE), and MMGBSA scores can be found in Table S1, while the 3D diagrams showing the superposition between the docked compounds in *Hs*DHODH and the crystal structure of *Hs*DHODH cocrystallized with brequinar (PDB ID: 1D3G) and teriflunomide (PDB ID: 1D3H) are available in Figure S1.

In addition to being more potent, lapachol also exhibits a higher electronic density potential, primarily concentrated in the 2-hydroxy-*p*-quinone portion, where the double bond is located (Figure 3). This is not observed in QHM020, which lacks the double bond and therefore reduces the electronic density potential in this region. Notably, the most potent compound of the 3-anilines-NQ series, QHM110, also
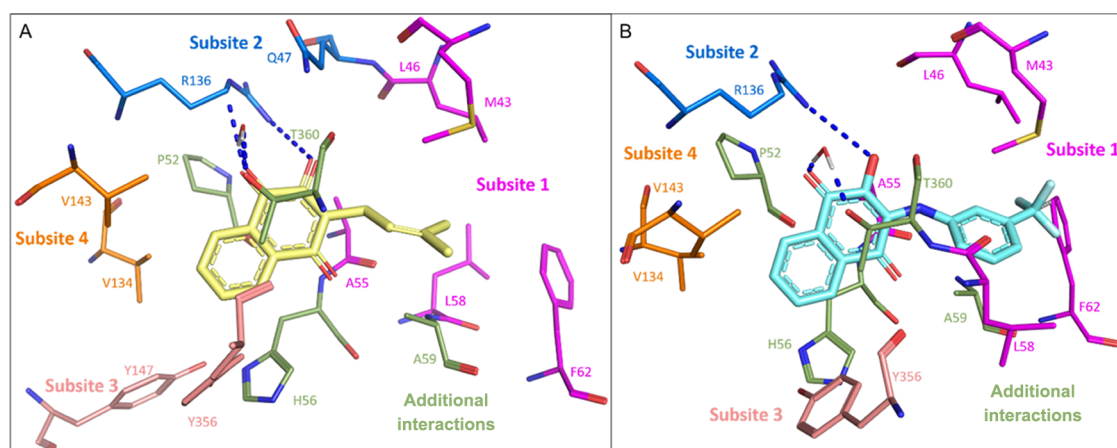
Figure 4. Quinones have the "brequinar-like" binding mode on *Hs*DHODH. Docked poses were obtained for (A) lapachol and (B) QHM110 (carbon atoms cyan). The subsites of the protein are colored according to Baumgartner's nomination,[40] subsite 1 (magenta), subsite 2 (dark blue), subsite 3 (salmon), and subsite 4 (orange). The quinones have additional interactions with hydrophobic residues, colored in green.

possesses a portion with high negative and positive electronic density potentials in the CF_3 position. To emphasize the significance of higher positive electron density groups in the isoprenyl or CF_3 position, which may have contributed to stronger interactions with the enzyme in the hydrophobic region, we have included 3D representations of docked lapachol and QHM110 with the molecular electrostatic surface of the protein in Figure S2. Interestingly, the higher electron density of the hydroxyquinone moiety in lapachol compared to the other compounds tested could be linked to stronger polar interactions with the molecular target, potentially resulting in higher inhibitory potency. It is noteworthy that QHM-0011 showed similar electronic density to lapachol, however, with lower potency, which could be due to any steric effect of the ortho-chloro substitution.

Molecular docking calculations indicated a good fit for all of the quinone compounds. Their superposition with brequinar and teriflunomide reveals a very similar interaction model for the docked compounds and brequinar, revealing this "brequinar-like" interaction pattern (Figure S1). According to Baumgartner's nomination,[40] all the quinones interact with subsites 1 (M43, L46, A55), 2 (R136), 3 (Y356), and 4 (V134, V143), and the same is observed for brequinar (PBDID 1D3G).[41] However, brequinar has additional residues involved in the interaction in subsites 1 (Y38, L42, L68, F58, F98, and M111) and subsite 5 (L67), a fact that can be related to the higher potency of brequinar (IC_{50} = 5.5 nM) compared to the tested quinones.

The quinones form an additional H-bond with T360 of *Hs*DHODH, mediated by a water molecule, which is not observed in brequinar and teriflunomide. This information suggests a chemical basis for the modulation of this target. The atomic strength depictions of the H-bonds were calculated and showed the higher importance of the H-bond with R136 and T360, being more predominant in QHM110 than in Lapachol, suggesting a greater stabilizing H-bond interaction with QHM110 (Figure S4).

Since the quinones have a "brequinar-like" interaction pattern with the enzyme and considering the adverse effects observed in clinical trials with brequinar,[42,43] we decided to assess the potential toxicity of these new molecules via *in vitro* cellular toxicity assays, which is a key point in drug discovery.[44] Cytotoxicity assays were performed on two different cell lines.

Naturally, we used Calu-3 cells, a pneumocyte lineage, to compare the antiviral effect, which was studied in this same cell type. Pneumocytes are the main cells affected during severe COVID-19. In addition, we also evaluated the cytotoxicity in cells of hepatic origin, the HepG2 cell line. Considering our future interest in developing these analogs for potential oral use, these substances would reach the liver via the hepatic portal circulation. Therefore, the cytotoxicity in liver cell lines was also evaluated. To that end, we used the approved drug teriflunomide as experimental control. Brequinar exhibited the lowest CC_{50} value (17 μM), whereas teriflunomide showed higher CC_{50} value (164 μM). The quinones QHM297 (17 μM) and lapachol (71 μM) also demonstrated high cytotoxicity. The other evaluated naphthoquinones exhibited lower cytotoxicity than the approved drugs (Table 1). We then conducted anti-SARS-CoV-2 assays in Calu-3 cells infected with SARS-CoV-2 to determine the EC_{50} values for the *Hs*DHODH inhibitors. The most potent anti-SARS-CoV-2 naphthoquinone was QHM230, which was also the most toxic. All the tested compounds exhibited an EC_{50} in the low micromolar range (Figure S3). The calculated selective index indicated that all tested quinone compounds were more selective than brequinar, suggesting that these compounds may cause fewer side effects than those observed with brequinar in several clinical studies.

Although all docked quinones show a binding mode similar to that of brequinar, there are some differences in the interactions of each docked molecule. By analyzing the most potent quinone against *Hs*DHODH, lapachol, and the most selective anti-SARS-CoV-2 compound, QHM110, we observed that the main interactions are preserved (Figure 4). However, slight differences in the inhibitory site could be responsible for the contrast in the biological assays. Lapachol (CC_{50} 71 μM) is much more cytotoxic than QHM110 (CC_{50} 178 μM), resulting in a selectivity difference of more than 2 times for the antiviral assays. Similar to the interaction pattern of brequinar compared to the tested quinones, lapachol has more hydrophobic interactions (14 interactions: A59, M43, L46, F62, L58, A55, G47, H56, P52, T360, V134, V143, Y147, Y356) compared to QHM110 (12 interactions: A59, M43, L46, F62, A55, H46, P52, T360, V134, V143, Y356, and L359), supporting the hypothesis that hydrophobic interactions are crucial for target modulation. However, the
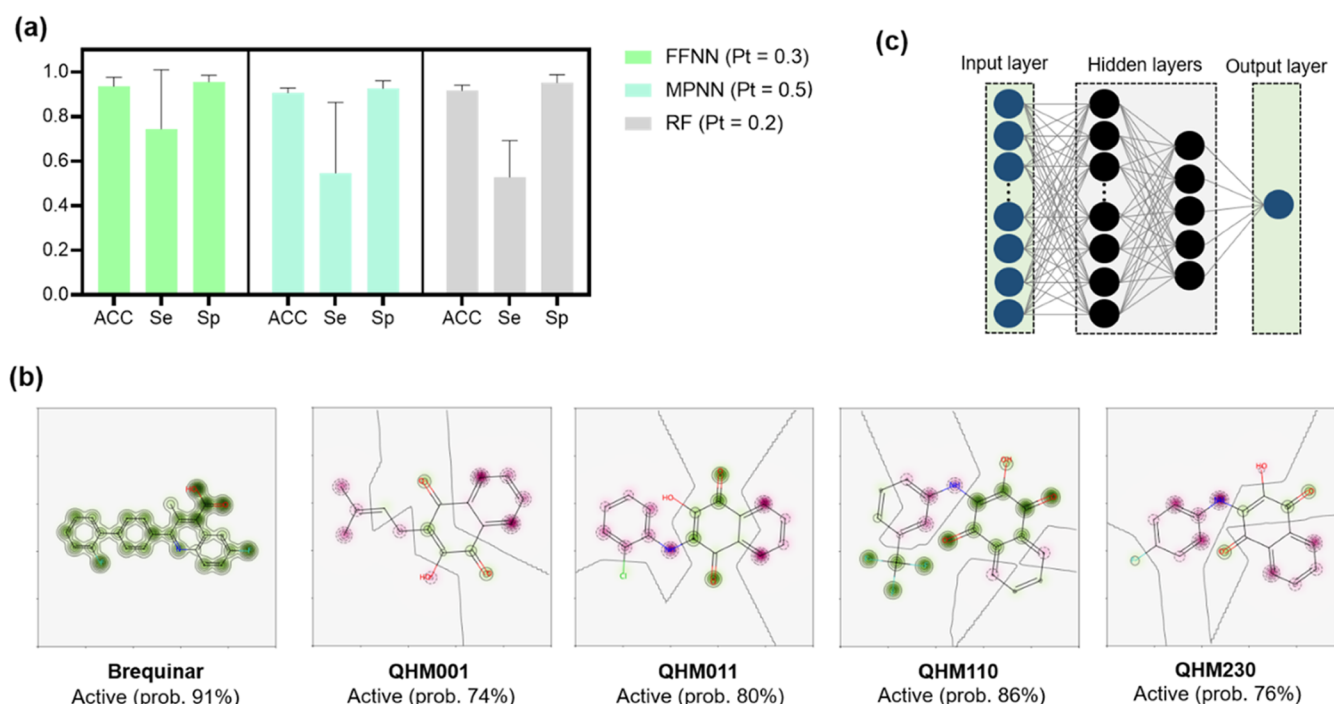
Figure 5. QSAR models for predicting compounds with antiviral activity. Panel (a) displays the statistical characteristics of the best classification models on the test sets, where higher values of ACC, SE, and SP indicate better performance. The optimal probability threshold (Pt) is also indicated. Models were developed utilizing a data set of 1,177 compounds evaluated for the cytopathic effect induced by SARS-CoV-2 infection in Vero E6 cells. The error bar represents the SD of the average performance over five splitting runs. Panel (b) shows the FFNN architecture used for classifying compounds as active or inactive against SARS-CoV-2. Panel (c) depicts the predicted influence probability maps of structural fragments for the experimental hits and brequinar effect on the antiviral activity generated from the best FFNN model. Fragments that promote positive contributions to the antiviral activity are highlighted in green, while those that decrease it are highlighted in pink.

participation of hydrophobic interactions seems to be related to cytotoxicity, as brequinar has more hydrophobic interactions than lapachol, which has more hydrophobic interactions than QHM110. This pattern is also observed in cytotoxicity and the hERG blockage prediction (see Table S4), when the structural divergence enhances the prediction between a possible blocker and nonblocker activity. This information could be valuable in guiding the synthesis of new molecules that are more promising in biological assays and potentially safer and more effective in the future.

To better understand the properties of our new brequinar-like molecules and prepare them for upcoming pharmacokinetic studies, we analyzed their water solubility. Water solubility holds significant importance in drug discovery, impacting dissolution rates and potentially influencing drug absorption and bioavailability.[45,46] For instance, high water solubility can lead to membrane permeability becoming the primary factor limiting biodistribution, overshadowing the role of solubility itself. According to the FDA's biopharmaceutical classification system guide,[47] a drug is considered highly soluble if its therapeutic dose dissolves in an aqueous medium of 250 mL, approximately one water glass. Brequinar, with a water solubility ranging from 0.5 to 0.7 μg/mL (DrugBank), falls into the category of low-solubility drugs. Consequently, it necessitates administration in high doses to compensate for the limited concentration available for absorption. Despite their similar molecular structures, the quinones exhibited different water solubility coefficients (Table S2). Interestingly, the quinones with the highest and lowest solubility coefficients were, respectively, QHM034 (100 μM) and QHM011 (3 μM), both of which are isomers of the chlorine-substituted aniline.

To assess the potential impact of solubility on the absorption of the tested quinones, we can assume the administration of 1 mg of the synthesized compounds, recognizing that formulation characteristics influence the effective therapeutic dose. In this context, for a drug to be considered highly soluble, its solubility should exceed 4 μg/mL. Applying this criterion, only QHM011, QHM020, and QHM230 demonstrated low solubility (Table S2). All other quinones showed water solubility that could be modulated with straightforward formulation strategies, such as preparing amorphous solid dispersions[48] or incorporating a low-toxic surfactant, such as Tween 80. This positions them as promising candidates for drug discovery campaigns. The addition of a low-toxic surfactant, like Tween 80, can effectively reduce interfacial tension, thereby improving the dispersibility of the compounds in biological mediums.[49,50] Another promising technique involves encapsulating the drugs in nanoparticles, enhancing their apparent solubility, and enabling sustained release.[51] Encapsulation strategies have demonstrated efficacy in improving drug solubility and bioavailability.[52]

In this study, we developed QSAR models for classifying untested compounds as either active or inactive with regard to phenotypic SARS-CoV-2 antiviral activity. Moreover, these models were developed with a focus on visually interpreting the fragments responsible for antiviral activity, emphasizing the specific molecular features that contribute to the observed activity of the active compounds. We used a data set comprising 1,177 compounds evaluated for the cytopathic effect induced by SARS-CoV-2 infection in Vero E6 cells and utilized machine learning and deep learning algorithms to train

and develop the models with the Extended Connectivity Fingerprints (ECFP) as chemical features.

Table S3 provides complete statistical characteristics of the training, validation, and test sets for the generated models. Figure 5a shows the statistical characteristics of the best classification models for the test sets. The closer the accuracy (ACC), sensitivity (SE), and specificity (SP) values are to 1, the better the model performed. As shown in Figure 5a, the feedforward neural network (FFNN) architecture outperformed the models obtained by graph representations (i.e., message-passing neural network) and machine learning (i.e., Random Forest). Our FFNN model exhibited the most balanced SE (0.7 ± 0.3) and SP (0.95 ± 0.02) values, indicating that the model can accurately detect both active and inactive compounds. The FFNN model was developed using a simple architecture (Figure 5b) consisting of two fully connected hidden layers with 10 and 3 units. Both layers were configured with a nonlinear Leaky ReLU activation function and dropout of 0.1 to prevent model overfitting.

The compounds identified as the best experimental hits in the cell-based assays with SARS-CoV-2, including lapachol, QHM011, QHM110, and QHM230, as well as the positive control brequinar, were evaluated using the best FFNN classification model. The high predictive power of the model was confirmed as all of the compounds in the study were correctly predicted as actives on SARS-CoV-2, with probabilities greater than 70%. Significant atomic and fragment features that prevent the cytopathic effect induced by SARS-CoV-2 were identified, providing structural insights for prospective hit-to-lead optimization. The results indicated that carbonyl and hydroxyl groups of the 2-hydroxy-1,4-naphthoquinone moiety positively contribute to the activity, which supports their importance as hydrogen bond acceptors, as previously suggested by molecular docking analyses. These features are highlighted in green in Figure 5c, while fragments that decrease the activity are shown in pink.

Therefore, the FFNN classification models developed in this study could be potentially applied in future studies aimed at discovering new compounds with anti-SARS-CoV-2 activity. The highlighted structural fragments in green could also serve as valuable guidance for optimization in subsequent studies. Additionally, all models, data, and codes used in this research are available on GitHub (https://github.com/LabMolUFG/COVID).

FINAL CONSIDERATIONS

The search for effective treatments against emerging and re-emerging viral diseases has become increasingly urgent in recent years, as drug-resistant strains and new viral variants continue to emerge. In this context, our study makes a substantial contribution to the field of antiviral drug discovery, focusing on the activity against SARS-CoV-2, the virus responsible for the COVID-19 pandemic. By applying a host-directed therapy approach targeting *Hs*DHODH, which plays a critical role in the *de novo* synthesis of pyrimidine nucleotides, we were able to inhibit viral replication and identify a series of naphthoquinones with potent anti-SARS-CoV-2 activity and low toxicity, suggesting their potential for further optimization and development. Additionally, we employed computational techniques like molecular docking and QSAR models using machine learning and deep learning algorithms to investigate the protein−ligand interactions and

identify the specific fragments responsible for the observed antiviral activity.

Notably, our study demonstrates that targeting *Hs*DHODH represents a promising strategy for antiviral drug discovery, as this host enzyme is less likely to cause resistance and is not associated with possible virus mutations. The host-directed therapy (HDT) approach, focusing on the DHODH target for the validation of antiviral compounds, has proven effective, particularly against RNA viruses like SARS-CoV-2. The HDT strategy is not commonly utilized for antiviral drugs in the market. Nonetheless, there are examples of approved medicines or candidates in clinical trials for HIV and HCV infections, such as DEBIO-025, a nonimmunosuppressive cyclosporin.[53] In the case of *Hs*DHODH inhibitors, their ability to inhibit DHODH, modulate immunity and inflammation, in addition to suppressing viral replication, suggests potential synergy with other antivirals to combat SARS-CoV-2.[54]

Our study represents a significant step forward in the search for effective treatments against viral diseases, and our findings could significantly impact the development of new antiviral drugs using an HDT approach.

■ METHODOLOGY

Inhibition Assays. The inhibitory assays were performed for indirect measure of dichlorophenol-indophenol (DCIP) reduction as previously described[39] in a 96-well microplate reader, in a reaction buffer containing 60 μM DCIP, 50 mM Tris pH 8.15, 150 mM KCl, 0.1% Triton X-100, 500 μM DHO, 100 μM CoQ0, and varied inhibitor concentrations previously incubated with the protein. At the starting point, different concentrations of the inhibitors (in 100% DMSO solution) were added to the *Hs*DHODH protein solution with a fixed DMSO percent of 10%. The reaction was started with the addition of 195 μL reaction buffer without inhibitor to 5 μL of *Hs*DHODH protein solution containing inhibitor, to a final concentration of 20 nM *Hs*DHODH and varied inhibitor concentrations. As a negative control, for each incubation time, 5 μL of the enzyme solution containing 10% DMSO was added to 195 μL of buffer, without the presence of the inhibitors. The reaction was monitored at 610 nm every 3 s throughout 60 s, in triplicate, for each concentration and for each tested compound. The reaction buffer without a protein solution was used as a blank for each point. The IC$_{50}$ was determined through the graph of the relative percent of inhibition concerning the negative control vs the log of the inhibitor concentration. The dose−response curve was fit according to eq 1 by using GraphPad Prism 5 software.

$$Y = 100/\left(1 + 10^{(X - \log \mathrm{IC}_{50})}\right) \tag{1}$$

Assessment of Cytotoxicity. The cytotoxicity of compounds was assessed by MTT (3-[4,5-dimethylthiazol-2-yl]-2,5-diphenyltetrazolium bromide) reduction assay to measure the metabolic reduction of MTT in the mitochondrial of HepG2 cell lines as previously described.[55] Cells were cultured at 5% CO$_2$ and 37 °C in DMEM medium with Streptomicyn (40 mg/L), supplemented with 10% heat-inactivated fetal bovine serum. Cells were seeded at a density of 1×10^3 cells/well in a 96-well plate prior to incubation with a serial dilution of compounds of interest for 72 h. Each compound's concentration was tested in triplicates. Cells were then incubated with 3-(4,5-dimethylthiazol-2-yl)-2,5-diphenyl-

tetrazolium bromide (Sigma-Aldrich M5655) for 4 h followed by formazan crystal solubilization with isopropanol and absorbance readings at OD_{570}. Cellular viability was expressed as a percentage relative to vehicle-treated control.

Monolayers of Calu-3 cells (2×10^4 cells/well) in 96-well culture plates were incubated with the compounds at different concentrations for 72 h at 37 °C at 5% CO_2. Each compound's concentration was tested in triplicates. Then, the supernatant was removed, the cells were washed with PBS and the monolayer was fixed/stained for 1 h at 37 °C, 5% CO_2 with methylene blue solution: HBSS + 1.25% glutaraldehyde +0.6% methylene blue (SYNTH). The solution was removed and the wells were washed lightly with distilled water. Subsequently, the elution solution (50% ethanol + 49% PBS + 1% acetic acid) was added and incubated for 15 min at room temperature. The volume was transferred to a flat-bottomed 96-well plate and the reading of absorbance was performed at a wavelength of 660 nm.

The CC_{50} was determined for both Calu-3 and Hep-G2 through the graph of the relative percent of cellular viability vs the log of compound concentration. The dose—response curve was fit according to eq 1 using GraphPad Prism 5 software.

Anti-SARS-CoV-2 Assays. *Cells, Viruses, and Reagents.* African green monkey kidney cells (Vero, subtype E6) and human lung epithelial cell lines (Calu-3) were expanded in high glucose DMEM High Glucose with 10% fetal bovine serum (FBS; Merck), with 100 U/mL penicillin and 100 μg/mL streptomycin (Pen/Strep; Gibco) at 37 °C in a humidified atmosphere with 5% CO_2. The SARS-CoV-2 B.1 lineage (GenBank accession number MT710714) was expanded in Vero E6 cells. Viral isolation was performed after a single passage in cell culture in 150 cm² flasks with high glucose DMEM plus 2% FBS. Observations for cytopathic effects were performed daily and peaked 4−5 days after infection. All procedures related to virus culture were handled in biosafety level 3 (BSL3) multiuser facilities according to WHO guidelines. Virus titers were determined as plaque-forming units (PFU/mL), and virus stocks were kept in −80 °C ultralow freezers.

The SARS-CoV-2 B.1 lineage (GenBank #MT710714) was isolated in Vero E6 cells from nasopharyngeal swabs of a confirmed case. All procedures related to virus culture were handled in the BSL3 multiuser facility at Fundação Oswaldo Cruz (FIOCRUZ), Rio de Janeiro, Brazil, according to World Health Organization (WHO) guidelines.[56]

Infections and Virus Titration. Calu-3 cells (2.0×10^5 cells/well) in 96-well plates (Nalge Nunc Institute, Rochester, NY) were infected with a multiplicity of infection (MOI) of 0.1 for 1 h at 37 °C at 5% CO_2. The inoculum was removed, and cells were incubated with treatments or not in DMEM with 10% FBS. After 48 h, the virus content in the supernatant was quantified by plaque-forming assays in Vero cells. For virus titration, monolayers of Vero E6 cells (2×10^4 cells/well) in 96-well plates were infected with serial dilutions of supernatants containing SARS-CoV-2 for 1 h at 37 °C. Semisolid high glucose DMEM medium containing 2% FBS and 2.4% carboxymethylcellulose was added, and cultures were incubated for 3 days at 37 °C. Then, the cells were fixed with 10% formalin for 2 h at room temperature. The cell monolayer was stained with 0.04% solution of crystal violet in 20% ethanol for 1 h. Plaque numbers were scored in at least 3 replicates per dilution by independent readers blinded to the experimental group. The virus titers were calculated by scoring for plaque-

forming units (PFU/mL), and nonlinear regression analysis of the dose—response curves were also performed to calculate the 50% effective concentration (EC_{50}). All experiments were carried out at least three independent times, including a minimum of two technical replicates in each assay. Data were analyzed using Prism GraphPad software 9.0 (Windows GraphPad Software, San Diego, CA). Values were presented as means ± standard deviations (SD).

Water Solubility Determination. The solubility of the synthesized compounds was determined in ultrapure water. An excess of each (1 mg) was added to beakers containing 1.5 mL of water, and the dispersions were kept at room temperature under stirring (IKA, Vortex 3, Staufen, Germany) for 12 h. Then, the samples were filtered in a PVDF membrane 0.22 μm and diluted in $DMSO/H_2O$ 1:1 for absorbance reading in a UV−vis spectrophotometer (Shimadzu, UV-1800, Kyoto, Japan). The study was conducted in triplicate for each drug.

Quartz cuvettes with 1 cm of the optical path were used for spectrophotometric quantification. Scans of known concentrations of the compounds were performed in $DMSO/H_2O$ 1:1, in the wavelength range (λ) between 220 and 600 nm, to determine the λ of maximum absorption (λmax) of each of them in the UV/vis. The λ_{max} was used to determine the solubility constant of the compounds from analytical calibration curves. The curves were constructed from known concentrations of the compounds in $DMSO/H_2O$ (1:1) in the concentration range from 0.1 to 10 μg/mL. Each concentration absorbance (A) was plotted on the ordered axis, and the respective concentration was on the abscissa's axis. The least-squares linear regression method was used to fit the data points. The first-order equation $A = ax + b$ (where a is the slope and b is the linear coefficient, given by the line intersection point with the ordinate axis) was used to convert the sample's A in concentration (x). Linear ranges were calculated using the linear correlation coefficient (r) as the minimum acceptable criterion of $r = 0.99$.

Computational Session. *Ligand Preparation.* The 3D structures of the quinones were drawn using ChemDraw software v.20.1.1, imported into Maestro workspace v.12.8 (Schrödinger, LCC, New York, 2021), and prepared using the LigPrep tool.[57,58] All ionization and tautomeric states were generated at pH 7.4 ± 0.5 using Epik software v.5.6 (Schrödinger, LCC, New York, 2021).[59,60] The lowest potential energy conformers and tautomers were calculated using OPLS4[61] and retained as input for docking studies.

Molecular Docking Calculations. The *Hs*DHODH structure in complex with the inhibitor 1214 (B6U) (PDB ID: 6LP6)[62] was selected based on a similarity between the cocrystallized ligand with the quinones, and the good resolution of 1.79 Å. The 3D structure of the protein was imported into the Maestro workspace and prepared using the Protein Preparation Wizard tool[58,60] (Schrödinger, LCC, New York, 2021). Hydrogen atoms were added, according to Epik v.5.6,[59,60] pK_a was calculated (pH 7.4 ± 0.5) using PROPKA,[63] and energy minimization was performed using the OPLS4 force field.[61] Then, a grid box of 15 Å around the Ubiquinone-binding site was generated using the receptor grid generation module of the Glide v. 9.1 (Schrödinger, LCC, New York, 2021) available on Maestro workspace (Schrödinger, LCC, New York, 2021),[64,65] using the cocrystallized ligand B6U and grid coordinates x, y, and z of −31.39, 21.81, 23.20 Å, respectively. The docking was performed using Glide software v.9.1,[64,65] using the extra-precision (XP),[66] to generate 10

poses for each ligand, and the Docking XP score. Then, the LE[67] was computed according to eq 2.

$$LE = \frac{(\text{docking score})}{(\text{number of heavy atoms})} \quad (2)$$

The Molecular mechanics with generalized Born and surface area solvation (MM-GBSA)[68] score was calculated using the Prime tool,[69−71] according to eq 3.[67]

$$MM\text{-}GBSA = \sum_{\text{bonds}} k_b \quad (3)$$

Finally, to analyze the protein−ligand interactions of the docking poses, we used PLIP server,[72] and for generating the images we used Pymol software v. 2.3.0.[73]

Molecular Electrostatic Potential. The electron density potential for the quinones was calculated using Gaussian software 09W revision D.01,[74] with theory AM1, basis 6-31G(d), single point, with multiplicity changed between 1−2, according with each quinone and Avogadro software v. 1.2,[75] was used to generate the electron density surfaces and color by electrostatic potential. For the *Hs*DHODH electrostatic surface, it was calculated using Pymol software v. 2.3.0,[73] with plugin APBS electrostatic, with all formal charges.

Hydrogen-Bond Strengths Calculation. The ability of hydrogen atoms to donate hydrogen bonds and the strength of atoms as acceptors in bonding interactions were calculated using the package Jazzy[76] implemented in Python v.3.6, an open-source tool for the prediction of hydrogen-bond strengths and free energies of hydration of small molecules.

hERG Blockage Prediction. The hERG blockage prediction was calculated using the Web server Pred-hERG v.5.0.[77,78]

QSAR Classification Models. The QSAR classification models based on machine learning and deep learning were developed in Python v.3.9 following best practices for predictive modeling.[79] To ensure the reproducibility of our computational workflow, all the source code and data sets used in this work can be found in our GitHub repository (https://github.com/LabMolUFG/COVID).

Data Curation. A data set of 9889 compounds with EC$_{50}$ data measuring cytopathic effect induced by SARS-CoV-2 in Vero E6 cells was collected and downloaded from the ChEMBL database (ID: CHEMBL4303835) and was used to develop the classification models. Briefly, all chemical structures and corresponding EC$_{50}$ data were carefully processed and curated according to the protocols proposed by Fourches et al.[80,81] During this step, an activity threshold of 10 μM was used to distinguish between active and inactive compounds since this value represents a good starting point for the prospective hit-to-lead optimization studies. Therefore, 107 compounds with EC$_{50} \leq 10$ μM were categorized as actives, whereas 4527 compounds with EC$_{50} > 10$ μM were categorized as inactives. Since the curated data set presented a high imbalance ratio of 1:42 (107 actives vs 4527 inactives), it was partially balanced (ratio of 1:10, 107 actives vs 1070 inactives) using a linear under-sampling approach.[80]

Machine Learning Model. The machine learning model was developed using the Random Forest (RF) algorithm implemented in Scikit-learn v.0.24.2 and Extended Connectivity Fingerprints with diameter 4 (ECFP4 with 2048 bits) implemented in RDKit v.2021.03.1. All models were built using 5-fold cross-validation approach, whereas their hyper-

parameters were optimized using a Bayesian approach implemented in Scikit-Optimize v.0.7.4.

Deep Learning Models. In this work, FFNN (using ECFP4 fingerprints as chemical features) and message-passing neural network (MPNN)[82] architectures were explored in Tensor-Flow v.2.8[83] to develop deep learning models. Initially, the curated data set was randomly divided into a training set, validation set, and test set at a ratio of 8:1:1 by Python scripts. The training set was used to build the model, the validation set for hyperparameter optimization, and the test set was used for the model evaluation. Concerning the complexity and high computational cost of explored architectures, we used a random searching strategy[83] based on previous experience for hyperparameter settings (e.g., dropout, learning rate, batch size, activation function, L1 and L2 regularization) and message-passing[83] hyperparameters (e.g., message units, message steps, number of attention heads). The early stopping approach[83] is used to avoid overfitting and save computational resources. The performance metrics of the validation set were used for the model selection.

Statistical Validation. The predictive performance of machine learning and deep learning models was evaluated using ACC, SE, SP, positive predictive value (PPV), negative predictive value (NPV), and the Matthews correlation coefficient (MCC). These metrics were calculated using eqs 4−9.

$$ACC = \frac{TP + TN}{N} \quad (4)$$

$$SE = \frac{TP}{TP + FN} \quad (5)$$

$$SP = \frac{TN}{TN + FP} \quad (6)$$

$$PPV = \frac{TP}{TP + FP} \quad (7)$$

$$NPV = \frac{TN}{TN + FN} \quad (8)$$

$$MCC = \frac{(TP \times TN - FP \times FN)}{\sqrt{(TP + FP)(TP + FN)(TN + FP)(TN + FN)}} \quad (9)$$

where N represents the number of compounds, FP and FN represent the number of false positives and false negatives, and TP and TN represent the number of true positives and true negatives, respectively.

Model Mechanistic Interpretation. Predicted probability maps were generated for the best QSAR model to visualize the fragment contributions for anticytopathic activity against SARS-CoV-2. Here, the "weight" of a fragment (bit) was considered as the predicted probability difference obtained when the bit is removed. The normalized weights were then used to color the atoms in a topography-like map with gray representing no changes in probability, green indicating a positive difference (i.e., the probability decreases when the bit is removed), and pink indicating a negative difference.[84]

■ ASSOCIATED CONTENT

Data Availability Statement

All models, data sets, and code are available on GitHub https://github.com/LabMolUFG/COVID.

Ⓢ Supporting Information

The Supporting Information is available free of charge at https://pubs.acs.org/doi/10.1021/acsomega.3c07845.

Superposition of all quinones docked in the *Hs*DHODH structure with the crystal structure of DHODH cocrystallized with brequinar and teriflunomide; 3D Conformations obtained by docking for *Hs*DHODH in complex with lapachol and QHM110; Anti-SARS-CoV-2 dose−response curves for all the tested compounds; Atomic strength depictions for the compounds Lapachol and QHM110; Molecular docking results; Experimental water solubility for the quinone compounds; Statistical characteristics of best QSAR models for the training, validation and test sets; Computational prediction of hERG blockage of the studied naphthoquinones and the known inhibitors brequinar and teriflunomide; and rational, synthesis, and characterization of the naphthoquinones (Chemistry Session). (PDF)

■ AUTHOR INFORMATION

Corresponding Authors

Carolina Horta Andrade − *Center for the Research and Advancement in Fragments and molecular Targets (CRAFT), School of Pharmaceutical Sciences at Ribeirao Preto, University of São Paulo, Ribeirão Preto 05508-060 SP, Brazil; Laboratory for Molecular Modeling and Drug Design (LabMol), Faculty of Pharmacy and Center for Excellence in Artificial Intelligence (CEIA), Institute of Informatics, Universidade Federal de Goiás, Goiânia 74605-170 GO, Brazil;* ⓘ orcid.org/0000-0003-0101-1492; Email: carolina@ufg.br

M. Cristina Nonato − *Protein Crystallography Laboratory, Department of Biomolecular Sciences, School of Pharmaceutical Sciences at Ribeirao Preto and Center for the Research and Advancement in Fragments and molecular Targets (CRAFT), School of Pharmaceutical Sciences at Ribeirao Preto, University of São Paulo, Ribeirão Preto 05508-060 SP, Brazil;* Email: cristy@fcfrp.usp.br

Authors

Aline D. Purificação − *Protein Crystallography Laboratory, Department of Biomolecular Sciences, School of Pharmaceutical Sciences at Ribeirao Preto and Center for the Research and Advancement in Fragments and molecular Targets (CRAFT), School of Pharmaceutical Sciences at Ribeirao Preto, University of São Paulo, Ribeirão Preto 05508-060 SP, Brazil;* ⓘ orcid.org/0000-0002-3127-7585

Sabrina Silva-Mendonça − *Center for the Research and Advancement in Fragments and molecular Targets (CRAFT), School of Pharmaceutical Sciences at Ribeirao Preto, University of São Paulo, Ribeirão Preto 05508-060 SP, Brazil; Laboratory for Molecular Modeling and Drug Design (LabMol), Faculty of Pharmacy, Universidade Federal de Goiás, Goiânia 74605-170 GO, Brazil*

Luiza V. Cruz − *Center for the Research and Advancement in Fragments and molecular Targets (CRAFT), School of Pharmaceutical Sciences at Ribeirao Preto, University of São Paulo, Ribeirão Preto 05508-060 SP, Brazil; Laboratory for*

Molecular Modeling and Drug Design (LabMol), Faculty of Pharmacy, Universidade Federal de Goiás, Goiânia 74605-170 GO, Brazil

Carolina Q. Sacramento − *Laboratory of Immunopharmacology, Oswaldo Cruz Institute and National Institute for Science and Technology on Innovation in Diseases of Neglected Populations (INCT/IDPN), Center for Technological Development in Health (CDTS), Fiocruz, Rio de Janeiro 21040-900 RJ, Brazil*

Jairo R. Temerozo − *Laboratory of Immunopharmacology, Oswaldo Cruz Institute, National Institute for Science and Technology on Innovation in Diseases of Neglected Populations (INCT/IDPN), Center for Technological Development in Health (CDTS), and National Institute for Science and Technology on Neuroimmunomodulation, Oswaldo Cruz Institute, Fiocruz, Rio de Janeiro 21040-900 RJ, Brazil*

Natalia Fintelman-Rodrigues − *Laboratory of Immunopharmacology, Oswaldo Cruz Institute and National Institute for Science and Technology on Innovation in Diseases of Neglected Populations (INCT/IDPN), Center for Technological Development in Health (CDTS), Fiocruz, Rio de Janeiro 21040-900 RJ, Brazil*

Caroline Souza de Freitas − *Laboratory of Immunopharmacology, Oswaldo Cruz Institute and National Institute for Science and Technology on Innovation in Diseases of Neglected Populations (INCT/IDPN), Center for Technological Development in Health (CDTS), Fiocruz, Rio de Janeiro 21040-900 RJ, Brazil*

Bruna Fleck Godoi − *Center for the Research and Advancement in Fragments and molecular Targets (CRAFT), School of Pharmaceutical Sciences at Ribeirao Preto, University of São Paulo, Ribeirão Preto 05508-060 SP, Brazil; Laboratory of Heterocyclic and Medicinal Chemistry (QHeteM), Department of Pharmaceutical Sciences, School of Pharmaceutical Sciences at Ribeirao Preto, University of São Paulo, Ribeirao Preto 05508-060 SP, Brazil*

Miguel Menezes Vaidergorn − *Center for the Research and Advancement in Fragments and molecular Targets (CRAFT), School of Pharmaceutical Sciences at Ribeirao Preto, University of São Paulo, Ribeirão Preto 05508-060 SP, Brazil; Laboratory of Heterocyclic and Medicinal Chemistry (QHeteM), Department of Pharmaceutical Sciences, School of Pharmaceutical Sciences at Ribeirao Preto, University of São Paulo, Ribeirao Preto 05508-060 SP, Brazil*

Juliana Almeida Leite − *Laboratory of Tropical Diseases, Department of Genetics, Evolution, Microbiology and Immunology, Institute of Biology, Unicamp, Campinas 13.083-857 SP, Brazil*

Luis Carlos Salazar Alvarez − *Laboratory of Tropical Diseases, Department of Genetics, Evolution, Microbiology and Immunology, Institute of Biology, Unicamp, Campinas 13.083-857 SP, Brazil*

Murillo V. Freitas − *Laboratory for Molecular Modeling and Drug Design (LabMol), Faculty of Pharmacy, Universidade Federal de Goiás, Goiânia 74605-170 GO, Brazil*

Meryck F. B. Silvac − *Laboratory for Molecular Modeling and Drug Design (LabMol), Faculty of Pharmacy and Laboratory of Cheminformatics, Faculty of Pharmacy, Universidade Federal de Goiás, Goiânia 74605-170 GO, Brazil;* ⓘ orcid.org/0000-0003-4969-3015

Bianca A. Martin − *Innovation Center in Nanostructured Systems and Topical Administration (NanoTop), School of*

Pharmaceutical Sciences at Ribeirao Preto, University of São Paulo, Ribeirão Preto 05508-060 SP, Brazil

Renata F. V. Lopez − *Innovation Center in Nanostructured Systems and Topical Administration (NanoTop), School of Pharmaceutical Sciences at Ribeirao Preto, University of São Paulo, Ribeirão Preto 05508-060 SP, Brazil;* ⊙ orcid.org/0000-0002-6448-6711

Bruno J. Neves − *Laboratory of Cheminformatics, Faculty of Pharmacy, Universidade Federal de Goiás, Goiânia 74605-170 GO, Brazil;* ⊙ orcid.org/0000-0002-1309-8743

Fabio T. M. Costa − *Laboratory of Tropical Diseases, Department of Genetics, Evolution, Microbiology and Immunology, Institute of Biology, Unicamp, Campinas 13.083-857 SP, Brazil*

Thiago M. L. Souza − *Laboratory of Immunopharmacology, Oswaldo Cruz Institute and National Institute for Science and Technology on Innovation in Diseases of Neglected Populations (INCT/IDPN), Center for Technological Development in Health (CDTS), Fiocruz, Rio de Janeiro 21040-900 RJ, Brazil*

Flavio da Silva Emery − *Center for the Research and Advancement in Fragments and molecular Targets (CRAFT), School of Pharmaceutical Sciences at Ribeirao Preto, University of São Paulo, Ribeirão Preto 05508-060 SP, Brazil; Laboratory of Heterocyclic and Medicinal Chemistry (QHeteM), Department of Pharmaceutical Sciences, School of Pharmaceutical Sciences at Ribeirao Preto, University of São Paulo, Ribeirao Preto 05508-060 SP, Brazil;* ⊙ orcid.org/0000-0002-8652-7123

Complete contact information is available at:
https://pubs.acs.org/10.1021/acsomega.3c07845

Author Contributions

C.H.A., F.d.S.E., and M.C.N. coordinated, designed, and supervised the project. C.H.A. and M.C.N. acquired funding for this project. B.F.G. and M.M.V. synthesized the compounds and organized the synthetic and structure elucidation experimental data. A.D.P. provided and organized the biochemical experimental data, and wrote the first draft of the manuscript. T.M.L.S. supervised and C.Q.S., J.R.T., and N.F-R. provided the data for the antiviral experiments and cytotoxicity data against the Calu-3 cell line. S.S.M., L.V.C., and M.V.F. provided molecular modeling data. M.F.B.S. and B.J.N. provided machine learning and deep learning models and developed GitHub repository. F.T.M.C. supervised and J.A.L. and L.C.S.A. provided the cytotoxicity data against the HepG2 cell line. R.F.V.L. supervised and B.A.M. provided compounds physicochemical data. All authors critically reviewed and contributed to the final version of the paper.

Notes

The authors declare no competing financial interest.

■ **ABBREVIATIONS**

ACC: accuracy

BSL3: biosafety level 3
DHO: dihydroorotate
DHODH: dihydroorotate dehydrogenase
DNA: DNA
FBS: fetal bovine serum
FDA: Food and Drug Administration
FFNN: feedforward neural network
FMN: flavin mononucleotide
*Hs*DHODH: human dihydroorotate dehydrogenase
LE: ligand efficiency
MCC: Matthews correlation coefficient
MM-GBSA: molecular mechanics with generalized Born and surface area solvation
MPNN: message-passing neural network
MTT: 3-[4,5-dimethylthiazol-2-yl]-2,5-diphenyltetrazolium bromide
NPV: negative predictive value
NQ: 2-hydroxynaphthoquinone
ORO: orotate
PFU: plaque-forming units
PPV: positive predictive value
QSAR: quantitative structure−activity relationship
RF: random forest
RNA: ribonucleic acid
SE: sensitivity
*Sm*DHODH: *Schistosoma mansoni* DHODH
SP: specificity
UMP: uridine monophosphate

■ **REFERENCES**

(1) Coronavirus Disease (COVID-19), 2019. https://www.who.int/emergencies/diseases/novel-coronavirus-2019.

(2) Tregoning, J. S.; Flight, K. E.; Higham, S. L.; Wang, Z.; Pierce, B. F. Progress of the COVID-19 vaccine effort: viruses, vaccines and variants versus efficacy, effectiveness and escape. *Nat. Rev. Immunol.* **2021**, *21* (10), 626−636.

(3) Li, M.; Wang, H.; Tian, L.; et al. COVID-19 vaccine development: milestones, lessons and prospects. *Signal Transduction Targeted Ther.* **2022**, *7* (1), 146.

(4) Coronavirus pandemic (COVID-19). *Our World in Data.* https://ourworldindata.org/coronavirus.

(5) Wang, L.-Y.; Cui, J. J.; Ouyang, Q. Y.; et al. Remdesivir and COVID-19. *Lancet* **2020**, *396* (10256), 953−954.

(6) Ferner, R. E.; Aronson, J. K. Remdesivir in covid-19. *BMJ* **2020**, *369*, m1610.

(7) McCreary, E. K.; Angus, D. C. Efficacy of Remdesivir in COVID-19. *JAMA* **2020**, *324* (11), 1041−1042.

(8) Kaur, H.; Sarma, P.; Bhattacharyya, A.; et al. Efficacy and safety of dihydroorotate dehydrogenase (DHODH) inhibitors "leflunomide" and "teriflunomide" in Covid-19: A narrative review. *Eur. J. Pharmacol.* **2021**, *906*, No. 174233.

(9) Reder, A. T.; Centonze, D.; Naylor, M. L.; et al. COVID-19 in Patients with Multiple Sclerosis: Associations with Disease-Modifying Therapies. *CNS Drugs* **2021**, *35* (3), 317−330.

(10) Rabie, A. M. Teriflunomide: A possible effective drug for the comprehensive treatment of COVID-19. *Curr. Res. Pharmacol. Drug Discovery* **2021**, *2*, No. 100055.

(11) Capone, F.; Motolese, F.; Luce, T.; et al. COVID-19 in teriflunomide-treated patients with multiple sclerosis: A case report and literature review. *Multiple Sclerosis Relat. Disord.* **2021**, *48*, No. 102734.

(12) Reynolds, E. S.; Lieberman, I.; Kornberg, A.; et al. The metabolism of orotic acid in aerobic bacteria. *J. Bacteriol.* **1955**, *69* (3), 250−255.

(13) Pardee, A. B.; Yates, R. A. Pyrimidine biosynthesis in *Escherichia coli. J. Biol. Chem.* **1956**, *221* (2), 743−756.

(14) Arakaki, T. L.; Buckner, F. S.; Gillespie, J. R.; et al. Characterization of Trypanosoma brucei dihydroorotate dehydrogenase as a possible drug target; structural, kinetic and RNAi studies. *Mol. Microbiol.* **2008**, *68* (1), 37−50.

(15) Reichard, P.; Soling, H.; Matikkala, E. J.; et al. The Enzymic Synthesis of Ureidosuccinic Acid in Rat Liver Mitochondria. *Acta Chem. Scand.* **1954**, *8*, 795−805.

(16) Knecht, W.; et al. Kinetics of inhibition of human and rat dihydroorotate dehydrogenase by quone, lawsone derivatives, brequinar sodium and polyporic acid. *Chem.−Biol. Interact.* **2000**, *124* (1), 61−76.

(17) Smith, L. H., Jr.; Baker, F. A. Pyrimidine metabolism in man. I. The biosynthesis of orotic acid. *J. Clin. Invest.* **1959**, *38* (5), 798−809.

(18) Ullrich, A.; Knecht, W.; Piskur, J.; et al. Plant dihydroorotate dehydrogenase differs significantly in substrate specificity and inhibition from the animal enzymes. *FEBS Lett.* **2002**, *529* (2−3), 346−350.

(19) Xiong, R.; Zhang, L.; Li, S.; et al. Novel and potent inhibitors targeting DHODH are broad-spectrum antivirals against RNA viruses including newly-emerged coronavirus SARS-CoV-2. *Protein Cell* **2020**, *11* (10), 723−739.

(20) Fairbanks, L. D.; et al. Importance of ribonucleotide availability to proliferating T-lymphocytes from healthy humans. Disproportionate expansion of pyrimidine pools and contrasting effects of de novo synthesis inhibitors. *J. Biol. Chem.* **1995**, *270* (50), 29682−29689.

(21) Hoffmann, H.-H.; Kunz, A.; Simon, V. A.; et al. Broad-spectrum antiviral that interferes with de novo pyrimidine biosynthesis. *Proc. Natl. Acad. Sci. U.S.A.* **2011**, *108* (14), 5777−5782.

(22) Qing, M.; Zou, G.; Wang, Q. Y.; et al. Characterization of dengue virus resistance to brequinar in cell culture. *Antimicrob. Agents Chemother.* **2010**, *54* (9), 3686−3695.

(23) (a) Froes, T. Q.; Zapata, L. C. C.; Akamine, J. S.; et al. DHODH Hot Spots: An Underexplored Source to Guide Drug Development Efforts. *Curr. Top. Med. Chem.* **2021**, *21* (23), 2134−2154. (b) Reis, R. A. G.; Calil, F. A.; Feliciano, P. R.; et al. The dihydroorotate dehydrogenases: Past and present. *Arch. Biochem. Biophys.* **2017**, *632*, 175−191.

(24) Huang, M.; Graves, L. M. De novo synthesis of pyrimidine nucleotides; emerging interfaces with signal transduction pathways. *Cell. Mol. Life Sci.* **2003**, *60* (2), 321−336.

(25) Lewis, T. A.; Sykes, D. B.; Law, J. M.; et al. Development of ML390: A Human DHODH Inhibitor That Induces Differentiation in Acute Myeloid Leukemia. *ACS Med. Chem. Lett.* **2016**, *7* (12), 1112−1117.

(26) Teschner, S.; Burst, V. Leflunomide: a drug with a potential beyond rheumatology. *Immunotherapy* **2010**, *2* (5), 637−650.

(27) Li, L.; Ng, S. R.; Colón, C. I.; et al. Identification of DHODH as a therapeutic target in small cell lung cancer. *Sci. Transl. Med.* **2019**, *11* (517), No. eaaw7852.

(28) Sykes, D. B.; Kfoury, Y. S.; Mercier, F. E.; et al. Inhibition of Dihydroorotate Dehydrogenase Overcomes Differentiation Blockade in Acute Myeloid Leukemia. *Cell* **2016**, *167* (1), 171−186.

(29) Miller, A. E. An updated review of teriflunomide's use in multiple sclerosis. *Neurodegener. Dis. Manage.* **2021**, *11* (5), 387−409.

(30) Boschi, D.; Pippione, A. C.; Sainas, S.; et al. Dihydroorotate dehydrogenase inhibitors in anti-infective drug research. *Eur. J. Med. Chem.* **2019**, *183*, No. 111681.

(31) Fu, H.; Zhang, Z.; Dai, Y.; et al. Brequinar inhibits enterovirus replication by targeting biosynthesis pathway of pyrimidines. *Am. J. Transl. Res.* **2020**, *12* (12), 8247−8255.

(32) Li, P.; Li, Y.; Wang, Y.; et al. Recapitulating hepatitis E virus-host interactions and facilitating antiviral drug discovery in human liver-derived organoids. *Sci. Adv.* **2022**, *8* (3), No. eabj5908.

(33) Park, J.-G.; Ávila-Pérez, G.; Nogales, A.; et al. Identification and Characterization of Novel Compounds with Broad-Spectrum Antiviral Activity against Influenza A and B Viruses. *J. Virol.* **2020**, *94* (7), No. e02149-19.

(34) Vasquez, D. M.; Park, J. G.; Ávila-Pérez, G.; et al. Identification of Inhibitors of ZIKV Replication. *Viruses* **2020**, *12* (9), 1041.

(35) Grigoryan, R.; Arabyan, E.; Izmailyan, R.; et al. Antiviral activity of brequinar against African swine fever virus infection in vitro. *Virus Res.* **2022**, *317*, No. 198826.

(36) Schnellrath, L. C.; Damaso, R. Potent antiviral activity of brequinar against the emerging Cantagalo virus in cell culture. *Int. J. Antimicrob. Agents* **2011**, *38* (5), 435−441.

(37) Li, S.-F.; Gong, M. j.; Sun, Y. f.; et al. Antiviral activity of brequinar against foot-and-mouth disease virus infection in vitro and in vivo. *Biomed. Pharmacother.* **2019**, *116*, No. 108982.

(38) Peres, R. S.; Santos, G. B.; Cecilio, N. T.; et al. Lapachol, a compound targeting pyrimidine metabolism, ameliorates experimental autoimmune arthritis. *Arthritis Res. Ther.* **2017**, *19* (1), 47.

(39) Calil, F. A.; David, J. S.; Chiappetta, E. R.; et al. Ligand-based design, synthesis and biochemical evaluation of potent and selective inhibitors of Schistosoma mansoni dihydroorotate dehydrogenase. *Eur. J. Med. Chem.* **2019**, *167*, 357−366.

(40) Baumgartner, R.; Walloschek, M.; Kralik, M.; et al. Dual binding mode of a novel series of DHODH inhibitors. *J. Med. Chem.* **2006**, *49* (4), 1239−1247.

(41) Liu, S.; Neidhardt, E. A.; Grossman, T. H.; et al. Structures of human dihydroorotate dehydrogenase in complex with antiproliferative agents. *Structure* **2000**, *8* (1), 25−33.

(42) Urba, S.; Doroshow, J.; Cripps, C.; et al. Multicenter phase II trial of brequinar sodium in patients with advanced squamous-cell carcinoma of the head and neck. *Cancer Chemother. Pharmacol.* **1992**, *31* (2), 167−169.

(43) Cramer, D. V. Brequinar sodium. *Transplant. Proc.* **1996**, *28* (2), 960−963.

(44) Mirahmad, M.; Sabourian, R.; Mahdavi, M.; et al. In vitro cell-based models of drug-induced hepatotoxicity screening: progress and limitation. *Drug Metab. Revi.* **2022**, *54* (2), 161−193.

(45) Liu, X.; Zhao, L.; Wu, B.; et al. Improving solubility of poorly water-soluble drugs by protein-based strategy: A review. *Int. J. Pharm.* **2023**, *634*, No. 122704.

(46) Stegemann, S.; Leveiller, F.; Franchi, D.; et al. When poor solubility becomes an issue: from early stage to proof of concept. *Eur. J. Pharm. Sci.* **2007**, *31* (5), 249−261.

(47) FDA. M9 Biopharmaceutics Classification System-Based Biowaivers, 2023. https://www.fda.gov/regulatory-information/search-fda-guidance-documents/m9-biopharmaceutics-classification-system-based-biowaivers.

(48) Vasconcelos, T.; Marques, S.; das Neves, J.; et al. Amorphous solid dispersions: Rational selection of a manufacturing process. *Adv. Drug Delivery Rev.* **2016**, *100*, 85−101.

(49) Park, S.; Mun, S.; Kim, Y. R.; et al. Influences of added surfactants on the water solubility and antibacterial activity of rosemary extract. *Food Sci. Biotechnol.* **2020**, *29*, 1373−1380.

(50) Mirgorodskaya, A. B.; Mamedov, V. A.; Zakharova, L. Y.; et al. Surfactant solutions for enhancing solubility of new arylquinolin-2-ones. *J. Mol. Liq.* **2017**, *242*, 732−738.

(51) Piroonpan, T.; Rimdusit, P.; Taechutrakul, S.; et al. pH-Responsive Water-Soluble Chitosan Amphiphilic Core-Shell Nanoparticles: Radiation-Assisted Green Synthesis and Drug-Controlled Release Studies. *Pharmaceutics* **2023**, *15* (3), 847.

(52) Mitchell, M. J.; Billingsley, M. M.; Haley, R. M.; et al. Engineering precision nanoparticles for drug delivery. *Nat. Rev. Drug Discovery* **2021**, *20* (2), 101−124.

(53) Paeshuyse, J.; Kaul, A.; De Clercq, E.; et al. The non-immunosuppressive cyclosporin DEBIO-025 is a potent inhibitor of hepatitis C virus replication in vitro. *Hepatology* **2006**, *43* (4), 761−770.

(54) Schultz, D. C.; Johnson, R. M.; Ayyanathan, K.; et al. Pyrimidine inhibitors synergize with nucleoside analogues to block SARS-CoV-2. *Nature* **2022**, *604* (7904), 134−140.

(55) Kumar, P.; Nagarajan, A.; Uchil, P. D.; et al. Analysis of Cell Viability by the MTT Assay. *Cold Spring Harbor Protoc.* **2018**, *2018* (6), No. e095505.

(56) Bain, W.; Lee, J. S.; Watson, A. M.; et al. Practical Guidelines for Collection, Manipulation and Inactivation of SARS-CoV-2 and COVID-19 Clinical Specimens. *Curr. Protoc. Cytometry* **2020**, *93* (1), No. e77.

(57) *Schrödinger Release 2023-2: LigPrep*; Schrödinger, LLC: New York, NY, 2023.

(58) Madhavi Sastry, G.; Adzhigirey, M.; Day, T.; et al. Protein and ligand preparation: parameters, protocols, and influence on virtual screening enrichments. *J. Comput.-Aided Mol. Des.* **2013**, *27* (3), 221−234.

(59) Shelley, J. C.; Cholleti, A.; Frye, L. L.; et al. Epik: a software program for pK(a) prediction and protonation state generation for drug-like molecules. *J. Comput.-Aided Mol. Des.* **2007**, *21* (12), 681−691.

(60) *Protein Preparation Wizard*; Schrödinger, LLC: New York, NY, 2021.

(61) Lu, C.; Wu, C.; Ghoreishi, D.; et al. OPLS4: Improving Force Field Accuracy on Challenging Regimes of Chemical Space. *J. Chem. Theory Comput.* **2021**, *17* (7), 4291−4300.

(62) Zuo, Z.; Liu, X.; Qian, X.; et al. Bifunctional Naphtho[2,3-*d*][1,2,3]triazole-4,9-dione Compounds Exhibit Antitumor Effects In Vitro and In Vivo by Inhibiting Dihydroorotate Dehydrogenase and Inducing Reactive Oxygen Species Production. *J. Med. Chem.* **2020**, *63* (14), 7633−7652.

(63) Olsson, M. H. M.; Søndergaard, C. R.; Rostkowski, M.; et al. PROPKA3: Consistent Treatment of Internal and Surface Residues in Empirical pKa Predictions. *J. Chem. Theory Comput.* **2011**, *7* (2), 525−537.

(64) *Schrödinger Release 2021-2: Glide*; Schrödinger, LLC: New York, NY, 2021.

(65) Halgren, T. A.; Murphy, R. B.; Friesner, R. A.; et al. Glide: a new approach for rapid, accurate docking and scoring. 2. Enrichment factors in database screening. *J. Med. Chem.* **2004**, *47* (7), 1750−1759.

(66) Friesner, R. A.; Murphy, R. B.; Repasky, M. P.; et al. Extra precision glide: docking and scoring incorporating a model of hydrophobic enclosure for protein-ligand complexes. *J. Med. Chem.* **2006**, *49* (21), 6177−6196.

(67) Hopkins, A. L.; Groom, C. R.; Alex, A.; et al. Ligand efficiency: a useful metric for lead selection. *Drug Discovery Today* **2004**, *9* (10), 430−431.

(68) Li, J.; Abel, R.; Zhu, K.; et al. The VSGB 2.0 model: a next generation energy model for high resolution protein structure modeling. *Proteins* **2011**, *79* (10), 2794−2812.

(69) Jacobson, M. P.; Friesner, R. A.; Xiang, Z.; et al. On the role of the crystal environment in determining protein side-chain conformations. *J. Mol. Biol.* **2002**, *320* (3), 597−608.

(70) Jacobson, M. P.; Pincus, D. L.; Rapp, C. S.; et al. A hierarchical approach to all-atom protein loop prediction. *Proteins* **2004**, *55* (2), 351−367.

(71) *Schrödinger Release 2021-2: Prime*; Schrödinger, LLC: New York, NY, 2021.

(72) Salentin, S.; Schreiber, S.; Haupt, V. J.; et al. PLIP: fully automated protein-ligand interaction profiler. *Nucleic Acids Res.* **2015**, *43* (W1), W443−W447.

(73) *The PyMOL Molecular Graphics System, Version 1.2r3pre*; Schrödinger, LLC: New York, NY, 2021.

(74) Frisch, M. J.; Trucks, G. W.; Schlegel, H. B.; Scuseria, G. E.; Robb, M. A.; Cheeseman, J. R.; Scalmani, G.; Barone, V.; Mennucci, B.; Petersson, G. A.; Nakatsuji, H.; Caricato, M.; Li, X.; Hratchian, H. P.; Izmaylov, A. F.; Bloino, J.; Zheng, G.; Sonnenberg, J. L.; Hada, M.; Ehara, M.; Toyota, K.; Fukuda, R.; Hasegawa, J.; Ishida, M.; Nakajima, T.; Honda, Y.; Kitao, O.; Nakai, H.; Vreven, T.; Montgomery, J. A., Jr.; Peralta, J. E.; Ogliaro, F.; Bearpark, M.; Heyd, J. J.; Brothers, E.; Kudin, K. N.; Staroverov, V. N.; Kobayashi, R.; Normand, J.; Raghavachari, K.; Rendell, A.; Burant, J. C.; Iyengar, S. S.; Tomasi, J.; Cossi, M.; Rega, N.; Millam, J. M.; Klene, M.; Knox, J. E.; Cross, J. B.; Bakken, V.; Adamo, C.; Jaramillo, J.; Gomperts, R.; Stratmann, R. E.; Yazyev, O.; Austin, A. J.; Cammi, R.; Pomelli, C.; Ochterski, J. W.; Martin, R. L.; Morokuma, K.; Zakrzewski, V. G.; Voth, G. A.; Salvador, P.; Dannenberg, J. J.; Dapprich, S.; Daniels, A. D.; Farkas, Ö.; Foresman, J. B.; Ortiz, J. V.; Cioslowski, J.; Fox, D. J. *Gaussian 09, Revision D.01*; Gaussian, Inc.: Wallingford, CT, 2009.

(75) Hanwell, M. D.; Curtis, D. E.; Lonie, D. C.; Vandermeersch, T.; Zurek, E.; Hutchison, G. R. Avogadro: An advanced semantic chemical editor, visualization, and analysis platform. *J. Cheminform.* **2012**, *4*, 17.

(76) Ghiandoni, G. M.; Caldeweyher, E. Fast calculation of hydrogen-bond strengths and free energy of hydration of small molecules. *Sci. Rep.* **2023**, *13* (1), No. 4143.

(77) Braga, R. C.; Alves, V. M.; Silva, M. F. B.; et al. Pred-hERG: A Novel web-Accessible Computational Tool for Predicting Cardiac Toxicity. *Mol. Inf.* **2015**, *34* (10), 698−701.

(78) Braga, R. C.; Alves, V.; Silva, M.; et al. Tuning HERG out: antitarget QSAR models for drug development. *Curr. Top. Med. Chem.* **2014**, *14* (11), 1399−1415.

(79) Tropsha, A. Best Practices for QSAR Model Development, Validation, and Exploitation. *Mol. Inf.* **2010**, *29* (6−7), 476−488.

(80) Fourches, D.; Muratov, E.; Tropsha, A.; et al. Trust, but verify: on the importance of chemical structure curation in cheminformatics and QSAR modeling research. *J. Chem. Inf. Model.* **2010**, *50* (7), 1189−1204.

(81) Fourches, D.; Muratov, E.; Tropsha, A.; et al. Trust, but Verify II: A Practical Guide to Chemogenomics Data Curation. *J. Chem. Inf. Model.* **2016**, *56* (7), 1243−1252.

(82) Gilmer, J.; Schoenholz, S. S.; Riley, P. F., et al. Neural Message Passing for Quantum Chemistry. *Proceedings of Machine Learning Research*, 2017, Vol. 70, pp 1263−1272.

(83) Abadi, M., et al. TensorFlow: a system for large-scale machine learning, 2023. https://www.scinapse.io/papers/2402144811.

(84) Riniker, S.; Landrum, G. A. Similarity maps - a visualization strategy for molecular fingerprints and machine-learning methods. *J. Cheminf.* **2013**, *5* (1), 43.